ACS APPLIED ENERGY MATERIALS

www.acsaem.org Article

Development of a Complex High-Conductivity Hole Transport Layer with Energy-Level Control for High-Efficiency Organic Solar Cells by the Solution Process

Hyoung Seok Lee, Yong Woon Han, Ye Chan Kim, Ji Youn Kim, Ji Hyeon Kim, and Doo Kyung Moon*

Cite This: https://doi.org/10.1021/acsaem.2c00960 Read Online

ACCESS | Metrics & More | Article Recommendations | Supporting Information

ABSTRACT: In this study, organic solar cells (OSCs) with a photoactive layer based on the bulk heterojunction structure of the high-performance polymer donor PM6 and non-fullerene acceptor BTP-eC9 were developed. Hydrogen molybdenum bronze (H_XMoO_3) was introduced as a hole transport layer (HTL) in lieu of poly(3,4-ethylenedioxythiophene)-polystyrene sulfonate (PEDOT:PSS), a common HTL in OSCs, for energy-level control and enhanced charge transport. UV photoelectron spectroscopy revealed that the highest occupied molecular orbital (HOMO) level of H_XMoO_3 (−5.10 eV) was lower than that of PEDOT:PSS (−5.00 eV). The V_{OC} of the OSC with H_XMoO_3 as the HTL (0.818 V) was higher than that of the device with PEDOT:PSS (0.636 V). By the energy-level alignment with enhanced V_{OC}, the energy conversion efficiency of the device with H_XMoO_3 (13.1%) was found to be higher than that of the device with PEDOT:PSS (8.4%). Ag nanowires (NWs) were added to the HTLs to improve their conductivity, and enhancements in electrical properties owing to increased intercontact due to the high conductivity of the NWs and their molecular rearrangement with H_XMoO_3 were determined. The increases in the short-circuit current density, fill factor, and open-circuit voltage of the fabricated PM6:BTP-eC9 device contributed to its outstanding properties, as demonstrated by its enhanced power conversion efficiency of 14.0%. The secondary binding and alignment of H_XMoO_3 and Ag NWs were determined by X-ray photoelectron spectroscopy and field-emission scanning electron microscopy, and the structure of the OSC was shown to improve carrier transport and interfacial contact. This work can provide a solution to address the low energy conversion efficiency of current OSCs and develop various applications.

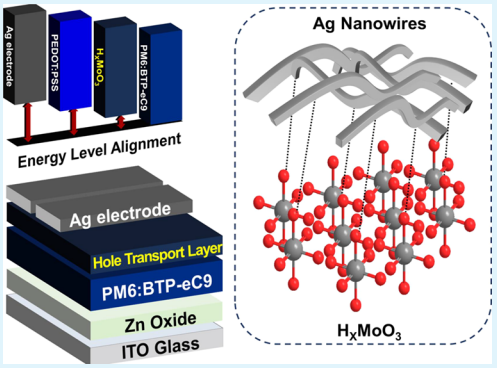

KEYWORDS: *organic solar cells, solution process, hole transport layer, metal nanowires, energy-level modification, conductivity, semi-transparent solar cells*

1. INTRODUCTION

Organic electronic devices are widely applied in various fields owing to their advantages of low cost, solution processability, and flexibility. Organic light-emitting diodes (OLEDs) and organic solar cells (OSCs), in particular, have attracted great research attention. These devices are composed of a multilayer structure with a photoactive layer and buffer layer between the metal electrodes. While OLEDs convert electrical energy into light energy, OSCs convert light energy into electrical energy. The active layers used for organic semiconductors differ from those used for inorganic semiconductors in that they exhibit a diversity of bandgaps based on their molecular structure. This feature enables the modification of the device structure to obtain high performance.[1−7] Recent studies on the control of visible-light absorption in organic semiconductor materials and research on transparent electrodes have led to the active investigation of transparent OSCs.[8−11]

OSCs have a bulk heterojunction (BHJ) structure consisting of an electron donor and acceptor. The active layer of this structure absorbs sunlight to form excitons which migrate to either side of the electrode through charge dissociation, extraction, and transport and exhibit photovoltaic characteristics. Many researchers have investigated the design and synthesis of electron donors and acceptors for OSCs. For instance, Jianhui and Yingping et al. reported an increase in power conversion efficiency (PCE) of over 15% when poly[(2,6-(4,8-bis(5-(2-ethylhexyl-3-fluoro)thiophen-2-yl)-benzo[1,2-b:4,5-b′]dithiophene))-alt-(5,5-(1′,3′-di-2-thienyl-5′,7′-bis(2-ethylhexyl)benzo[1′,2′-c:4′,5′-c′]dithiophene-4,8-dione)] (PM6) was used as the donor and 2,2′-((2Z,2″Z)-((12,13-bis(2-ethylhexyl)-3,9-diundecyl-12,13-dihydro-[1,2,5]-thiadiazolo[3,4-*e*]thieno[2,″3:″4′,5′]thieno[2′,3′:4,5]pyrrolo-

Received: March 29, 2022
Accepted: June 3, 2022

[3,2-*g*]thieno[2′,3′:4,5]thieno[3,2-*b*]indole-2,10-diyl)bis-(methanylylidene))bis(5,6-difluoro-3-oxo-2,3-dihydro-1*H*-indene-2,1-diylidene))dimalononitrile (Y6, E_{gopt} = 1.81 eV) was used as the acceptor.[12,13]

The energy level is a critical factor for maximizing the efficiency of photovoltaic devices, such as OSCs, because it is closely related to parameters that determine performance, such as interfacial alignment, absorption, and electrical properties. An electrode and active layer may be sufficient for the basic operation of OSCs, but the barrier formed by the considerable energy-level gap between the electrode and active layer may interfere with charge transport. The barrier problem can be solved by introducing a buffer layer with a suitable energy level between the electrode and active layer. This buffer layer can also improve interfacial contact by forming a fine morphology between these components.[14−21]

The PCE of OSCs can be enhanced in several ways, such as (1) adopting suitable donors and acceptors as photovoltaic active materials, (2) introducing additives into the active layer to arrange ordered crystallinity,[22,23] and (3) controlling the alignment of interlayer energy levels using buffer layers [e.g., hole transport layer (HTL), electron transport layer (ETL), and so forth] with varying energy levels within the device. Numerous studies on this topic have been conducted following the development of Y6.[24,25] The formation of new energy levels can be promoted by inducing structural changes to donors and acceptors, such as by introducing various functional groups to their molecular structures.[26,27] In general, the energy level can be reduced by introducing an atom or a molecule with high electronegativity.[28] ETLs and HTLs, such as ZnO and poly(3,4-ethylenedioxythiophene)-polystyrene sulfonate (PEDOT:PSS), respectively, can be used as buffer layers for OSCs.

The presence of PEDOT:PSS in the buffer layer may enhance the efficiency of an OSC because the electrical properties and surface characteristics of this material can be controlled to achieve high conductivity, wetting property, and processibility.[29] However, the acidic properties of PEDOT may reduce device stability by eroding the electrode and, eventually, the active layer over time.[30] The hygroscopic properties of water/alcohol-based PEDOT:PSS, which absorbs moisture from the air, may also reduce the long-term stability of the device. Several studies have been performed by different research teams to overcome these limitations. For instance, the acidity of PEDOT:PSS could be reduced by post-treatment or the addition of different solvents.[31,32] Such studies demonstrate that the acidity of the buffer layer may be effectively reduced to improve device stability; however, the corresponding decline in conductivity usually leads to decreases in efficiency as a serious side effect.[33,34] Moreover, despite its suitability for solution processing, PEDOT:PSS has lower efficiency compared with conventional MoO_3-deposited devices, which greatly limits its applications.

Differences in the energy level of recently reported active layer materials with low HOMO levels could lead to decreases in efficiency. Thus, a strategy to match the energy levels of active layer materials with deep energy levels, such as energy-level tuning, is necessary. Several scholars have performed studies on the integration of various materials with PEDOT:PSS.[26,35−40]

Research on the preparation of buffer bi-layers, introduction of a metal complex layer, or creation of a hybrid buffer layer through the direct introduction of other materials has been actively conducted. The most commonly introduced metal complexes are those containing a transition metal, such as Mo, V, W, or Ni.[41−48] Studies on the introduction of metal nanowires (NWs) to compensate for the inherently low short-circuit current density (J_{SC}) observed during solution processing in comparison with that obtained during deposition processing have also been reported. The excellent conductivity of metal NWs promotes the interaction between the photoactive layer and electrode to achieve improved charge transfer and interfacial contact.[49,50]

In the present study, molybdenum hydrogen bronze (H_XMoO_3) HTLs were synthesized to achieve energy-level tuning in OSCs. Ag NWs were then integrated with the HTLs to obtain hybrid HTLs that could enhance the current density of these devices. The active layers of the OSCs consisted of a BHJ-structured PM6:BTP-eC9 binary D/A-type system. The properties of the obtained devices were then evaluated after their preparation.

2. EXPERIMENTAL SECTION

2.1. Materials. ITO glass (sheet resistance, 10 Ω) was purchased from AMG (Korea). Zinc acetate dehydrate, 2-methoxymethanol, chlorobenzene (CB), Mo powder, isopropyl alcohol (IPA, HPLC grade), and hydrogen peroxide (H_2O_2, 30%) were purchased from Sigma-Aldrich (USA). PM6 and (2,2′-[[12,13-bis(2-butyloctyl)-12,13-dihydro-3,9-dinonylbisthieno[2,″3:″4′,5′] thieno[2′,3′:4,5]-pyrrolo[3,2-e:2′,3′-g][2,1,3]benzothiadiazole-2,10-diyl] bis[methylidyne(5,6-chloro-3-oxo-1*H*-indene-2,1(3H)-diylidene)]] bis-[propanedinitrile]) (BTP-eC9) were purchased from Derthon (China). 1,8-Diiodooctane (DIO) was purchased from Alfa-Aesar (USA). PEDOT:PSS (Clevios HTL Solar) was purchased from Heraeus (Germany). Ag NWs were purchased from SG Flexio (Korea). The top Ag electrode was prepared using Ag granules purchased from iTASCO (Korea).

2.2. Preparation of the HTL Solutions. Reference HTL 1 was formed by mixing PEDOTPSS and IPA in 1:1 volume ratio. Mo powder was added to 10 mL of IPA to obtain a 10 mg mL^{-1} solution and magnetically stirred at room temperature to prepare reference HTL 2. After 10 min, 0.35 mL of H_2O_2 was added to the Mo solution, and magnetic stirring was continued for over 40 h. As the reaction proceeded, the color of the solution changed from gray to yellow, green, and blue.[51] The hybrid HTLs 1, 2 were formed by mixing each reference HTL 1, 2 with Ag NWs in 95:5 volume ratio.

2.3. Device Fabrication. Prior to the experiments, the ITO glass was sequentially ultrasonicated with acetone, detergent, IPA, and deionized water. The glass was then annealed and cleaned using a UV/O_3 cleaner. An ETL was formed on the ITO glass after cleaning. Briefly, ZnO sol−gel was prepared from a mixture of zinc acetate, 2-methoxyethanol, and ethanol amine and then spin-coated under ambient conditions to induce thin-film formation. The ETL was formed by thermal annealing on a hot plate at 150 °C for 1 h. The photoactive layer was produced using PM6 as the donor and BTP-eC9 as the acceptor at a mass ratio of 1:1.2 in a solution of CB (1,8-DIO, 0.5 vol%). The prepared solution was spin-coated in a glove box, and the photoactive layer was formed through thermal annealing. Next, solutions of PEDOT:PSS and H_XMoO_3 were spin-coated under ambient conditions, and the HTLs were formed by drying. The top Ag electrode was formed by thermal deposition (thickness, 100 nm) using a vacuum evaporator under a pressure of 1×10^{-6} torr and a deposition rate of 2.5 Å s^{-1}.

2.4. Device Characterization. The energy conversion efficiency and characteristics of the OSCs produced in this study were assessed using a Keithley 2400 source measure unit. A solar simulator (Oriel, 1000 W) was used as the light source, and the intensity of incident light was set based on a reference silicon solar cell measured under AM 1.5 G and 100 mW cm^{-2}, as suggested by the National Renewable Energy Laboratory. The external quantum efficiency of the

https://doi.org/10.1021/acsaem.2c00960
ACS Appl. Energy Mater. XXXX, XXX, XXX−XXX

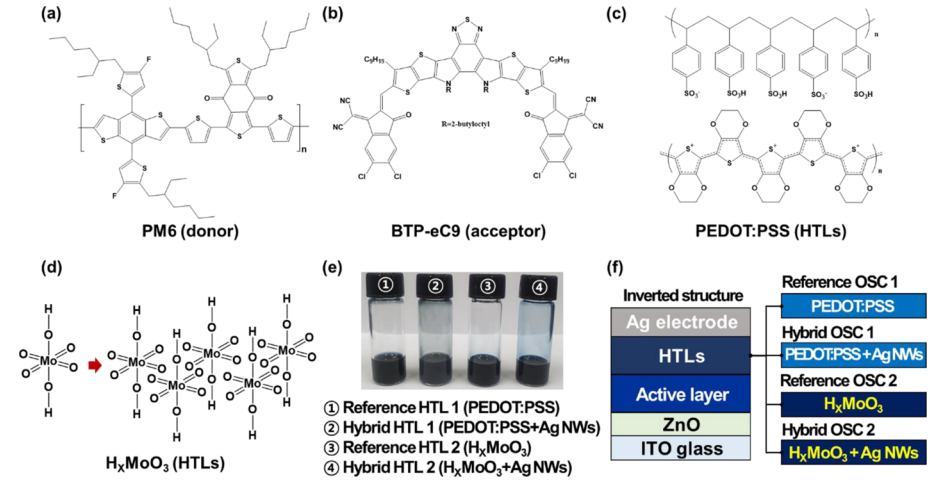

Figure 1. Molecular structures of (a) PM6, (b) BTP-eC9, (c) PEDOT:PSS, and (d) H_XMoO_3. (e) Images of the HTL solutions. (f) Structure of the fabricated device bearing HTLs.

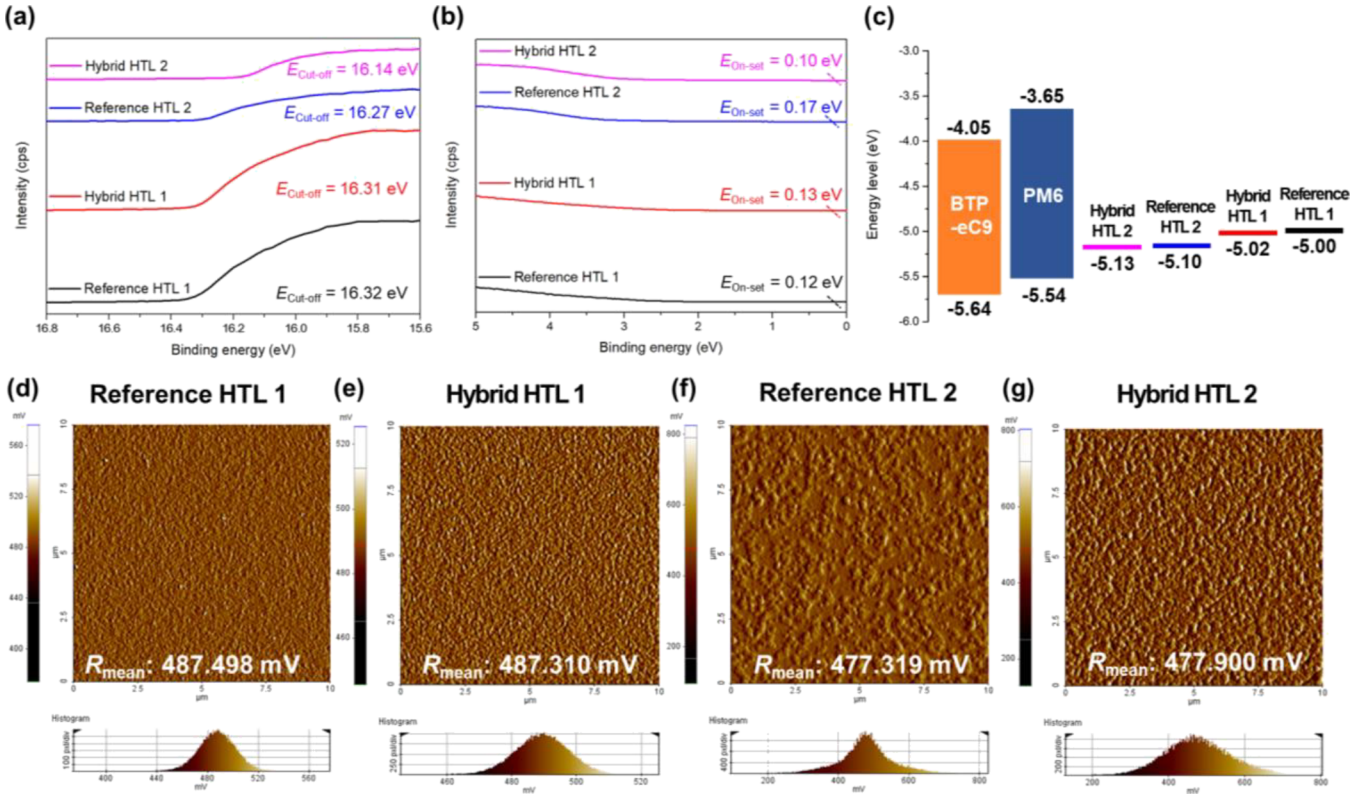

Figure 2. UPS characteristics of the HTLs. (a) cut-off energy, (b) on-set energy, and (c) calculated energy-level alignment of the HTLs. EFM amplitude images of (d) reference HTL 1, (e) hybrid HTL 1, (f) reference HTL 2, and (g) hybrid HTL 2

fabricated OSCs was measured using a Polaronix K3100 IPCE measurement system (Mac Science), which allowed for the measurement of the incident PCE. UV photoelectron spectroscopy (UPS) and X-ray photoelectron spectroscopy (XPS) were performed using a Micro X-Ray/UV photoelectron spectroscope with a He I light source (21.2 eV) developed by the Korea Basic Science Institute. Atomic force microscopy (AFM) and electric force microscopy (EFM) were conducted using a PSIA XE-100 instrument. A high-resolution field-emission scanning electron microscope (SU8010, Hitachi) was used for surface and cross-sectional field-emission scanning electron microscopy (FESEM) and energy-dispersive X-ray spectroscopy (EDS). Contact angles (CAs) were measured using a CA analyzer (DSA100, KRUSS). The 3C beamline of the Pohang Accelerator Laboratory was used for grazing-incident wide-angle X-ray scattering (GIWAXS) studies. The GIWAXS sample was fabricated such that the active layer, HTLs, was formed on silicon wafers by the spin-coating method. The materials' solutions are the same as the experiment.

3. RESULTS AND DISCUSSION

3.1. Properties of the Photoactive Layer and HTLs.

Figure 1 shows images of (a) PM6 as the polymer donor in the photoactive layer, (b) BTP-eC9 as the non-fullerene acceptor, (c) PEDOT:PSS as the HTL, (d) molecular structure of H_XMoO_3, (e) images of the prepared HTL solutions, and (f) structure of the fabricated OSCs.

https://doi.org/10.1021/acsaem.2c00960
ACS Appl. Energy Mater. XXXX, XXX, XXX−XXX

Table 1. Energy-Level Data of the HTLs from UPS Analysis

hole transport layer	$E_{Cut\text{-}off}$ (eV)	$E_{On\text{-}set}$ (eV)	HOMO level (eV)
1. Reference HTL 1 (PEDOT:PSS)	16.32	0.12	−5.00
2. Hybrid HTL 1 (PEDOT:PSS + Ag NWs)	16.31	0.13	−5.02
3. Reference HTL 2 (H_XMoO_3)	16.27	0.17	−5.10
4. Hybrid HTL 2 (H_XMoO_3 + Ag NWs)	16.14	0.10	−5.13

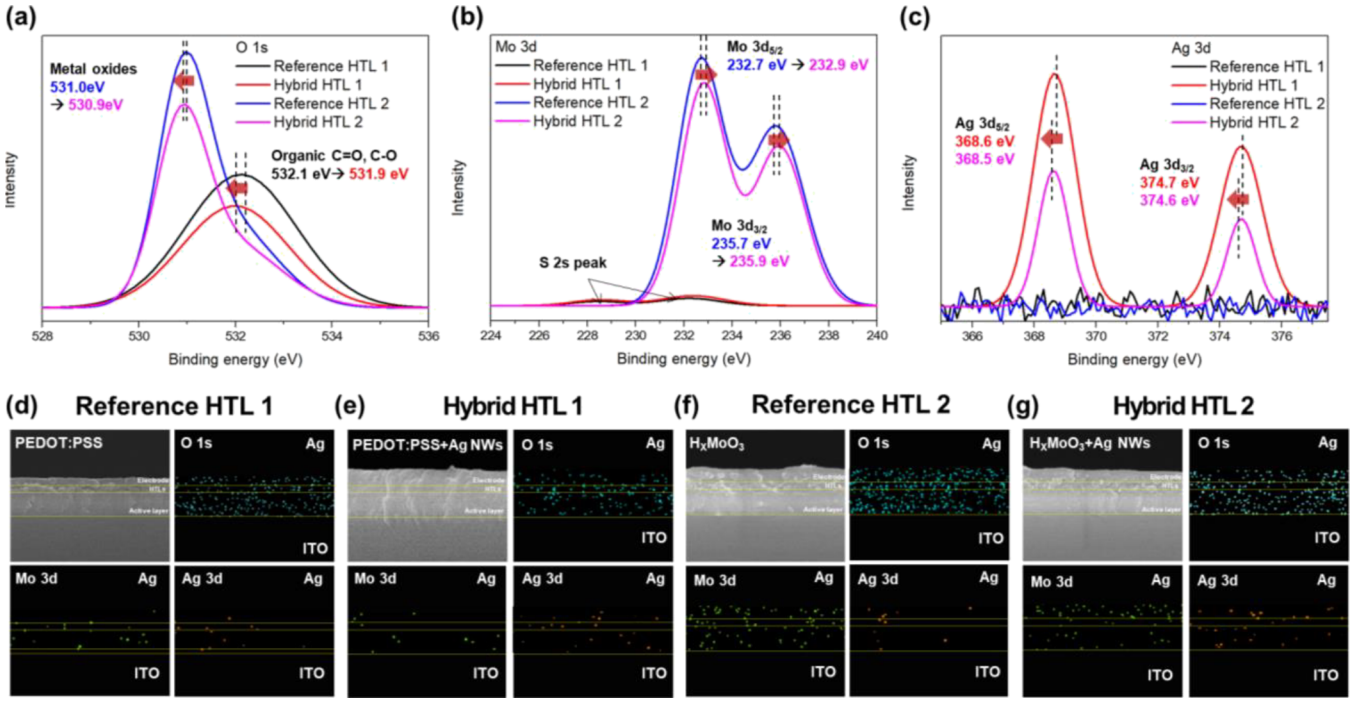

Figure 3. Surface XPS characteristics of the HTLs: (a) O 1s, (b) Mo 3d, and (c) Ag 3d signals. Cross-sectional FE-SEM and EDS mappings of (d) reference HTL 1, (e) hybrid HTL 1, (f) reference HTL 2, and (g) hybrid HTL 2

3.2. Energy Level and Electrical Characteristics. Figure 2 and Table 1 show the UPS data for the HTLs prepared in this study and the energy levels of the materials estimated from the UPS analysis, respectively. Based on the UPS results, the $E_{cut\text{-}off}$ values (Figure 2a) of reference HTL 1 (PEDOT:PSS), hybrid HTL 1 (PEDOT:PSS + Ag NWs), reference HTL 2 (H_XMoO_3), and hybrid HTL 2 (H_XMoO_3 + Ag NWs) were 16.32, 16.31, 16.27, and 16.14 eV, respectively. Among the HTLs prepared, hybrid HTL 2 showed the lowest $E_{on\text{-}set}$, followed by reference HTL 1, hybrid HTL 1, and reference HTL 2 (Figure 2b). Thus, the HOMO energy level (−21.2 eV + $E_{cut\text{-}off}$ − $E_{on\text{-}set}$) of hybrid HTL 2 was the deepest, followed by those of reference HTL 2, hybrid HTL 1, and reference HTL 1 (Figure 2c).[52,53] When compared with those of the other HTLs, the energy-level variations in the HTL integrated with Ag NWs decreased. Thus, an energy level that was well-matched to that of PM6 (E_{HOMO} = −5.54 eV) was created, and the energy barrier formed between the active layer and electrode was effectively ameliorated to achieve a high V_{OC}.[47]

Figure 2d−g presents the EFM amplitude data of the prepared HTLs. The measured amplitudes of reference HTL 1, hybrid HTL 1, reference HTL 2, and hybrid HTL 2 were 487.498, 487.310, 477.319, and 477.900 mV, respectively. Compared with that of PEDOT:PSS, the surface potential of H_XMoO_3 was lower. The surface potential of the photoactive layer used in this study was 489.900 mV (Figure S1). A high built-in potential could promote the formation of a more suitable electric field on H_XMoO_3 to enhance its energy level and carrier-transport properties.[16] This finding agrees with the UPS results.[54,55]

3.3. Atomic Signal and Molecular Arrangement Analysis. Figures 3a−c and S2 present the surface XPS data for the prepared HTLs. The measured C 1s signals and S 2p signals are shown in Figure S2a,2b, respectively. The S 2p signals of reference HTL 1 and hybrid HTL 1 (Figure S2b) indicate that decreases in J_{SC} lead to increases in the PSS peak.[47,56,57] The O 1s signals of PEDOT:PSS and H_XMoO_3 (Figure 3a) indicated the presence of organic C═O and C−O at 532.1 eV and the metal oxide at 531.0 eV. When Ag NWs were integrated with the HTLs, the binding energies of PEDOT:PSS and H_XMoO_3 blue-shifted by 0.1 and 0.2 eV, respectively, and the peaks showed a low intensity. This result was attributed to the interaction of the HTLs with the NWs.

The Mo 3d spectrum of the PEDOT:PSS film shown in Figure 3b revealed the weak signals of sulfate at 228.5 and 232.3 eV. The MoO_3 peak of the H_XMoO_3 film was detected at 232.7 ∼ 9 and 235.7 ∼ 9 eV. The addition of Ag NWs led to a 0.2 eV red shift in the binding energies, and the peaks showed a low intensity. This result was attributed to the reduction of Mo due to interactions with the added NWs.

The Ag 3d spectra in Figure 3c revealed the peaks of metal Ag at 368.6 and 374.7 eV for the hybrid HTL 1 film and 368.5 and 374.6 eV for the hybrid HTL 2 film. Moreover, the binding energies of the latter shifted by 0.1 eV with a low intensity when compared with those of the former. This finding may be attributed to the oxidation of Ag due to

https://doi.org/10.1021/acsaem.2c00960
ACS Appl. Energy Mater. XXXX, XXX, XXX−XXX

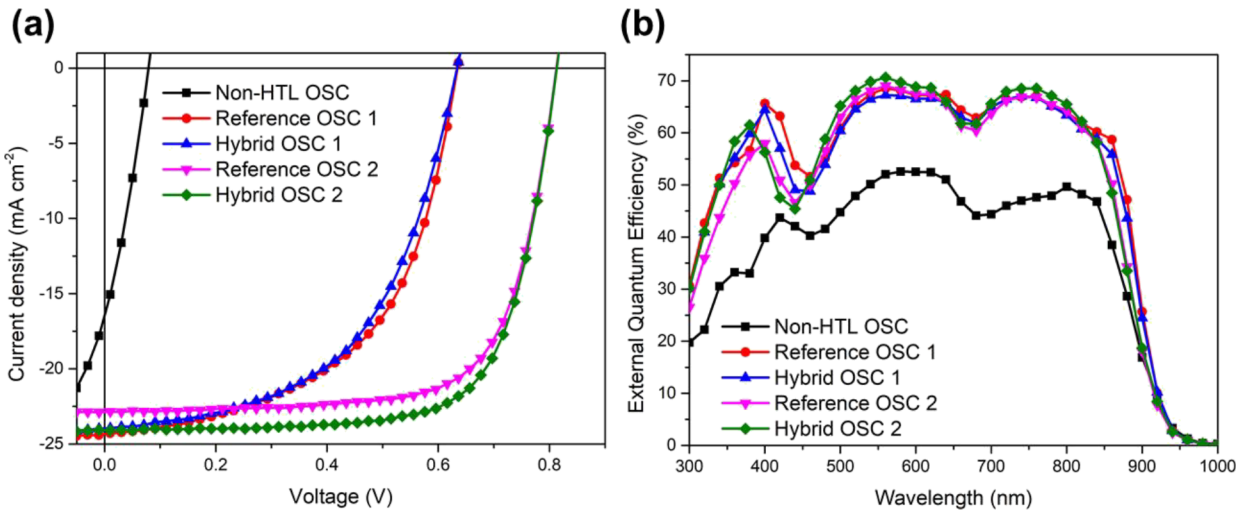

Figure 4. (a) $J-V$ and (b) external quantum efficiency (EQE) characteristics of fabricated devices bearing HTLs based on the photoactive layer PM6:BTP-eC9.

Table 2. Photovoltaic Performance of Fabricated Devices Bearing HTLs Based on PM6:BTP-eC9 after Optimization[a]

photoactive layer	hole transport layer	J_{SC} (mA cm^{-2})	V_{OC} (V)	FF (%)	PCE (%)
PM6:BTP-eC9	1. HTL X (None)	17.8	0.07	29.3	0.3
	2. Reference HTL 1 (PEDOT:PSS)	24.4	0.636	54.0	8.4
	3. Hybrid HTL 1 (PEDOT:PSS + Ag NWs)	24.0	0.636	53.5	8.2
	4. Reference HTL 2 (H_XMoO_3)	22.9	0.818	70.2	13.1
	5. Hybrid HTL 2 (H_XMoO_3 + Ag NWs)	24.1	0.818	71.0	14.0

[a]Devices were fabricated with an inverted structure (ITO/ZnO/photoactive layer/HTLs/Ag, active area = 0.04 cm^2).

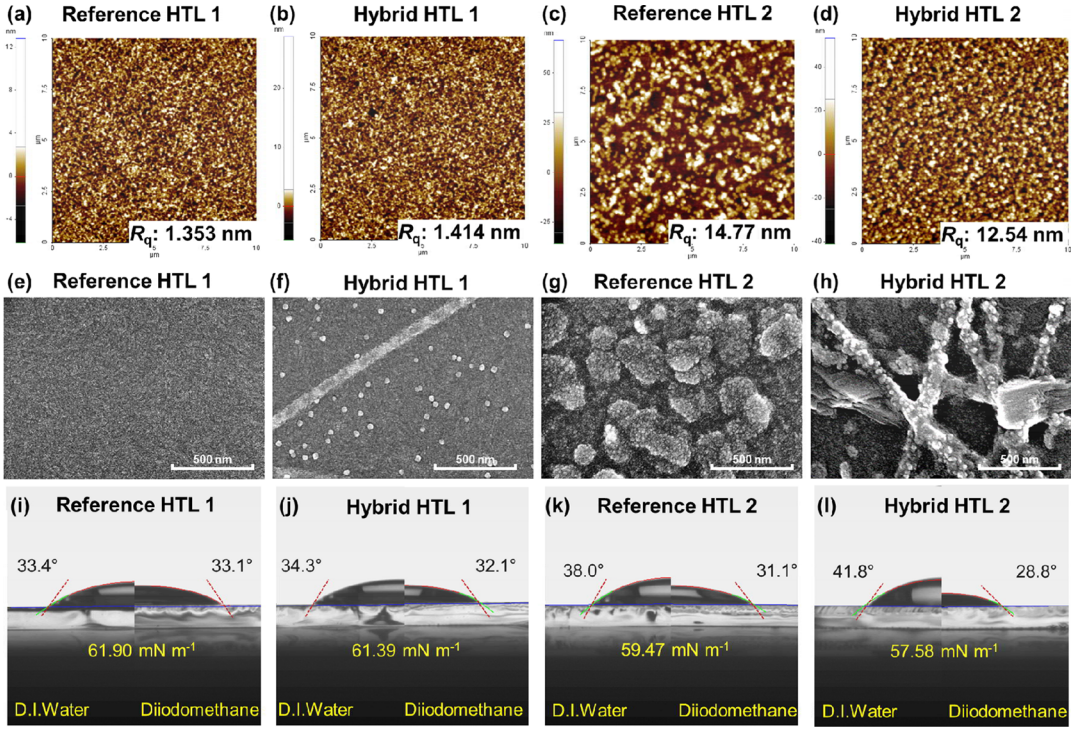

Figure 5. Surface morphological characteristics of (a) reference HTL 1, (b) hybrid HTL 1, (c) reference HTL 2, and (d) hybrid HTL 2 and SEM data of (e) reference HTL 1, (f) hybrid HTL 1, (g) reference HTL 2, and (h) hybrid HTL 2. Surface contact angles of (i) reference HTL 1, (j) hybrid HTL 1, (k) reference HTL 2, and (l) hybrid HTL 2.

interactions between the NWs and H_XMoO_3. The XPS analysis also indicated the occurrence of secondary binding between H_XMoO_3 and the Ag NWs.

Figure 3d–g presents the cross-sectional FE-SEM and EDS mapping data for the devices prepared with reference HTL 1, hybrid HTL 1, reference HTL 2, and hybrid HTL 2. EDS

https://doi.org/10.1021/acsaem.2c00960
ACS Appl. Energy Mater. XXXX, XXX, XXX−XXX

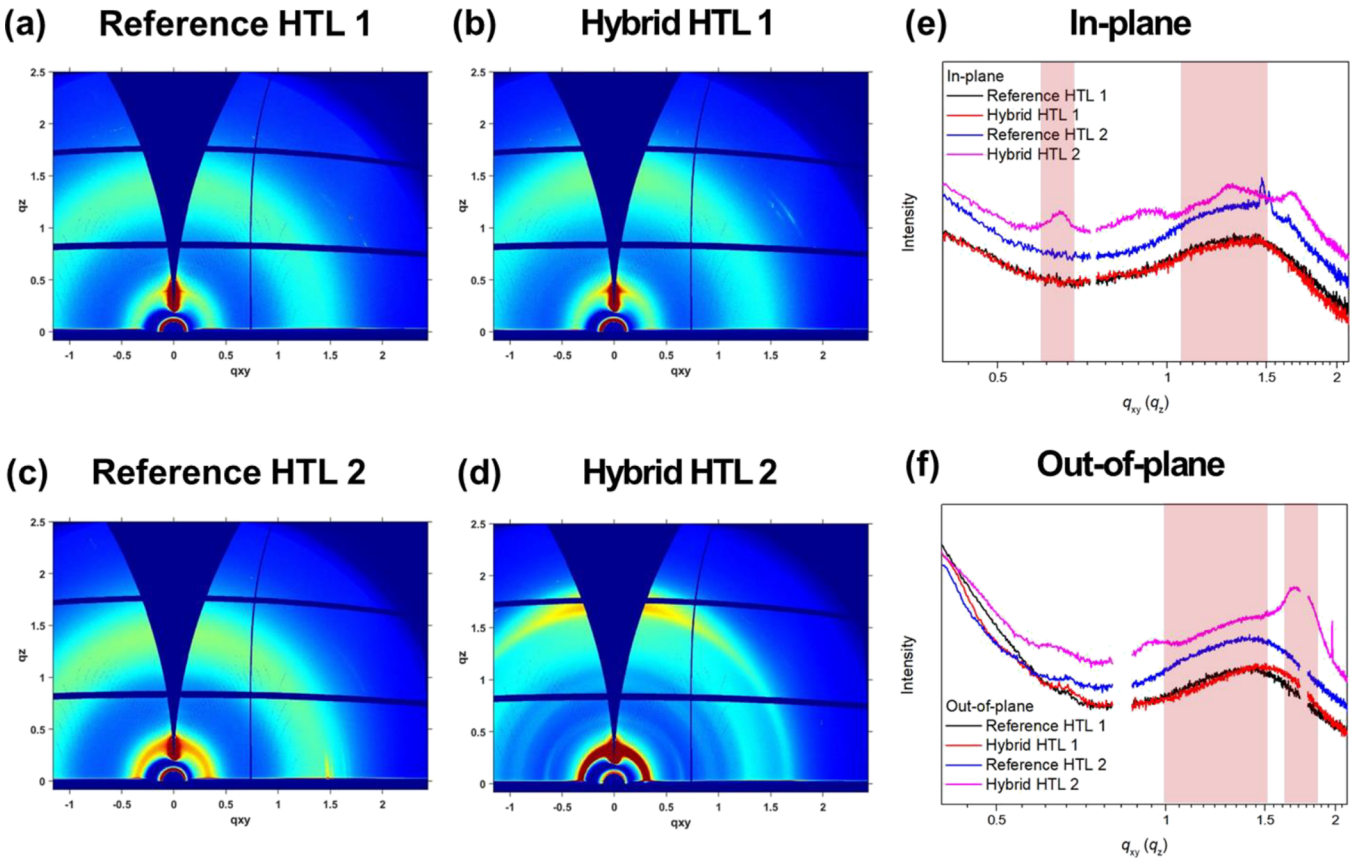

Figure 6. GIWAXS characteristics of (a) reference HTL 1, (b) hybrid HTL 1, (c) reference HTL 2, and (d) hybrid HTL 2. Line-cut profiles of the HTL materials in the (e) in-plane and (f) out-of-plane directions.

analysis of the O 1s, Mo 3d, and Ag 3d signals was performed to identify the molecular orientations of PEDOT:PSS, H_XMoO_3, and Ag NWs, respectively. The reference HTL 1 and hybrid HTL 1 film showed lower distributions of the O 1s signal compared with the reference HTL 2 and hybrid HTL 2 films. This finding confirms that the O 1s signal decreases after the introduction of Ag NWs to these films. The hybrid HTL 2 film showed higher distributions of the Mo 3d signal at the upper part of the active layer and lower part of the HTL compared with the reference HTL 2 film. The hybrid HTL 2 film showed higher distributions of the Ag 3d signal at the upper part of the HTL and lower part of the Ag electrode compared with the hybrid HTL 1 film. Although the cross-sectional FE-SEM results did not clearly define the binding mode and structure of the hybrid HTL 1 film, the structure of the hybrid HTL 2 film, wherein the Ag NWs and H_XMoO_3 occupied the upper and lower parts, respectively, of the HTL, can be seen. This finding indicates that the energy-level alignment effect of H_XMoO_3 is exerted on the upper part of the active layer, and increased conductivity and interfacial contact due to the Ag NWs occur at the lower part of the Ag electrode.[58]

3.4. Photovoltaic Properties of the Fabricated OSCs. The photovoltaic performance of the developed devices is presented in Figure 4 and Table 2. The device with PEDOT:PSS as the reference HTL 1 showed a PCE of 8.4% (J_{SC} = 24.4 mA cm^{-2}, V_{OC} = 0.636 V, FF = 54.0%). The PCE of the device with hybrid HTL 1 decreased to 8.2% (J_{SC} = 24.0 mA cm^{-2}, V_{OC} = 0.636 V, FF = 53.5%), which could be attributed to decreases in its J_{SC} and FF. The device with reference HTL 2 showed a PCE of 13.1% (J_{SC} = 22.9 mA cm^{-2}, V_{OC} = 0.818 V, FF = 70.2%). The decrease in J_{SC} but substantial increases in V_{OC} and FF of this device contributed to its high PCE. This finding agrees with the UPS results of the HTL, which indicated the formation of a well-matched energy level between H_XMoO_3 and the photoactive layer. The PCE of the device with hybrid HTL 2 was 14.0% (J_{SC} = 24.1 mA cm^{-2}, V_{OC} = 0.818 V, FF = 71.0%).

3.5. Nano-Structural and Surface Morphological Characteristics. The AFM results are presented in Figures 5a–d and S3. Figure S3 shows the root mean square (RMS) roughness (0.969 nm) of the photoactive layer (PM6:BTP-eC9) used in this study. The reference HTL 1 film in Figure 5a showed an RMS roughness of 1.353 nm. By comparison, the hybrid HTL 1 film in Figure 5b showed an RMS roughness of 1.414 nm, which indicated a change in the surface morphology of the film following the introduction of the Ag NWs. The RMS roughness of the reference HTL 2 film in Figure 5c, at 14.77 nm, was higher than that of the reference HTL 1 film owing to the larger domain-size characteristics of metal oxides. This increase in surface roughness may lead to the lower J_{SC} (24.0 mA cm^{-2}) of the hybrid HTL 1 film compared with that of the reference HTL 1 film. The RMS roughness of the hybrid HTL 2 film in Figure 5d decreased to 12.54 nm following the introduction of the Ag NWs. This finding indicates an improvement in surface morphology, which could decrease carrier recombination and enhance the J_{SC} (24.1 mA cm^{-2}) of the film.

Figure 5e–h presents the surface FE-SEM results of the HTL materials. In Figure 5e, the reference HTL 1 film showed

https://doi.org/10.1021/acsaem.2c00960
ACS Appl. Energy Mater. XXXX, XXX, XXX–XXX

smooth surface characteristics in line with the AFM results. The FE-SEM image of the hybrid HTL 1 film in Figure 5f indicated the presence of surface Ag NWs, but binding between the NWs and PEDOT:PSS was not observed. The FE-SEM image of the reference HTL 2 film in Figure 5g showed the formation of a large domain of metal oxides, in contrast to the surface of the reference HTL 1 film. In Figure 5h, the hybrid HTL 2 film showed surface Ag NWs similar to those found in the hybrid HTL 1 film; binding between H_XMoO_3 and the Ag NWs was also observed.[59] Moreover, the surface of the sample was smoother compared with that obtained before the introduction of the NWs. This result coincides with the XPS and cross-sectional FE-SEM results and could be attributed to the interaction between H_XMoO_3 and Ag NWs, which leads to increases in J_{SC} and FF.

The surface CA analysis results are presented in Figure 5i–l. As shown in Figure 5i, the reference HTL 1 film had CAs of 33.4° (water) and 33.1° (diiodomethane), with a surface energy of 61.90 mN m^{-1}. The CAs of the hybrid HTL 1 film in Figure 5j were 34.3° (water) and 32.1° (diiodomethane), with a surface energy of 61.39 mN m^{-1}. These results reveal the formation of a more hydrophobic surface following the introduction of the Ag NWs. The surface of the reference HTL 2 film in Figure 5k was more hydrophobic than that of the reference HTL 1 film. Specifically, the CAs of the reference HTL 2 film were 38.0° (water) and 31.1° (diiodomethane), with a surface energy of 59.47 mN m^{-1}. The hybrid HTL 2 film, shown in Figure 5l, revealed the most hydrophobic surface among the HTL films following the introduction of the Ag NWs; this film showed CAs of 41.8° (water) and 28.8° (diiodomethane), with a surface energy of 57.58 mN m^{-1}. This finding coincides with the XPS and cross-sectional FE-SEM results. The enhanced interfacial contact and increased phase separation of this film were due to the binding and alignment of H_XMoO_3 and Ag NWs in the lower and upper parts, respectively, of the film.[47,60]

The results of GIWAXS are presented in Figure 6a–f. In the case of the reference HTL 1 film (Figure 6a), a (100) peak was detected at 0.3 $Å^{-1}$ in the in-plane direction, a broad amorphous peak was detected at 1.28–1.5 $Å^{-1}$, and a (010) peak with characteristic π–π stacking was detected at 1.0–1.5 $Å^{-1}$ in the out-of-plane direction.[61] The intensity of the (010) peak of the hybrid HTL 1 film in Figure 6b was stronger than that of the reference HTL 1 film, indicating an increase in the face-on structure.[19,47,62,63] The intensity of the (010) peak of the reference HTL 2 film (Figure 6c) in the out-of-plane direction was stronger than that of the reference HTL 1 film, which could be attributed to the ordered stacking of the H_XMoO_3 structures, as shown in Figure 1d. The characteristics of the reference HTL 2 film introduced with Ag NWs are shown in Figure 6d. The strong intensity of the (010) peak of the hybrid HTL 1 film in Figure 6b confirmed that the face-on structure increased. The GIWAXS results indicate that enhancements in the J_{SC} of hybrid HTL 2 are due to improvements in its π–π stacking.[64]

A semi-transparent OSC device was fabricated, and its photovoltaic performance was measured. The results are presented in Figure S4 and Table S1. The performance of the device with PEDOT:PSS as the reference HTL 1 was 7.8% (J_{SC} = 19.5 mA cm^{-2}, V_{OC} = 0.676 V, FF = 69.0%). By comparison, the performance of the device with hybrid HTL 1 was 7.2% (J_{SC} = 19.1 mA cm^{-2}, V_{OC} = 0.636 V, FF = 69.3%). While the FF of this device increased, the decrease in its J_{SC} led to a decrease in its efficiency. The semi-transparent device with H_XMoO_3 as the reference HTL 2 showed a remarkable increase in PCE and energy conversion efficiency of 9.9% (J_{SC} = 19.5 mA cm^{-2}, V_{OC} = 0.818 V, FF = 61.8%) compared with the reference HTL 1 device. The addition of Ag NWs further increased the efficiency of the device to 10.2% (J_{SC} = 20.1 mA cm^{-2}, V_{OC} = 0.818 V, FF = 61.8%); thus, the energy conversion efficiency of this device is higher than that of the device consisting solely of H_XMoO_3. The reference HTL 1 and reference HTL 2 devices similarly showed improvements in transmittance from 15.8 to 16.1% and from 15.1 to 15.7%, respectively, following the addition of the Ag NWs. This finding may be attributed to improvements in face-on characteristics, as illustrated in the GIWAXS results.

The histogram of the PCE values of the devices and box plot of PCE are presented in Figure S5. Each OSC was fabricated more than 20 devices.

4. CONCLUSIONS

In this study, H_XMoO_3 and Ag NWs were introduced as HTLs in lieu of PEDOT:PSS to OSCs based on BHJ-structured PM6/BTP-eC9 as a photoactive layer.

A recent trend in OSC research is the development of devices bearing photoactive layers with deep HOMO levels. However, the use of PEDOT:PSS, the conventional solution-processing HTL, could lead to drastic reductions in V_{OC} due to energy-level mismatches.

UPS analysis showed that the HOMO level of H_XMoO_3 was approximately −5.13 to −5.10 eV, which is lower than that of PEDOT:PSS (−5.02 to −5.00 eV). This finding indicates that the energy barrier, which could cause reductions in V_{OC}, may be ameliorated by the formation of a more suitable energy level with PM6/BTP-eC9, which features a deep HOMO level. XPS and FE-SEM confirmed the secondary binding and alignment of H_XMoO_3 and Ag NWs, and the resulting structure enhanced carrier transport and interfacial contact.

The OSC produced with H_XMoO_3 as the HTL demonstrated a higher V_{OC} of 0.818 V compared with the device using PEDOT:PSS as the HTL (0.636 V), as well as an increase in energy conversion efficiency from 8.4 to 13.1%. Characterization of the OSC device hybridized with Ag NWs and H_XMoO_3 as the HTL also showed improvements in J_{SC} from 22.9 to 24.1 mA cm^{-2}, which confirmed its increased energy conversion efficiency.

The results collectively suggested that the development of a semi-transparent OSC device could lead to an enhanced energy conversion efficiency of 10.2% and an average visible transmittance (λ = 380–780 nm) of 15.7%. The potential applications of integrated OSCs may be verified in future studies on solution-processed HTLs for high-performance semi-transparent and flexible OSC modules.

■ ASSOCIATED CONTENT

Supporting Information

The Supporting Information is available free of charge at https://pubs.acs.org/doi/10.1021/acsaem.2c00960.

Experimental data of the EFM amplitude, surface XPS characteristics of the HTLs, J–V curves, UV transmittance of semi-transparent OSCs, and AFM measurements (PDF)

https://doi.org/10.1021/acsaem.2c00960
ACS Appl. Energy Mater. XXXX, XXX, XXX–XXX

AUTHOR INFORMATION

Corresponding Author

Doo Kyung Moon − *Nano and Information Materials Laboratory, Department of Chemical Engineering, Konkuk University, Seoul 05029, Republic of Korea;* orcid.org/0000-0001-9482-7508; Phone: +82-2-450-3498; Email: dkmoon@konkuk.ac.kr; Fax: +82-2-444-0765

Authors

Hyoung Seok Lee − *Nano and Information Materials Laboratory, Department of Chemical Engineering, Konkuk University, Seoul 05029, Republic of Korea;* orcid.org/0000-0001-6369-4175

Yong Woon Han − *LX Hausys, Seoul 07796, Republic of Korea*

Ye Chan Kim − *Nano and Information Materials Laboratory, Department of Chemical Engineering, Konkuk University, Seoul 05029, Republic of Korea*

Ji Youn Kim − *Nano and Information Materials Laboratory, Department of Chemical Engineering, Konkuk University, Seoul 05029, Republic of Korea*

Ji Hyeon Kim − *Nano and Information Materials Laboratory, Department of Chemical Engineering, Konkuk University, Seoul 05029, Republic of Korea*

Complete contact information is available at: https://pubs.acs.org/10.1021/acsaem.2c00960

Author Contributions

All of the authors contributed to writing this manuscript and approve of its final version.

Notes

The authors declare no competing financial interest.

ACKNOWLEDGMENTS

This research was supported by Konkuk University in 2018.

REFERENCES

(1) Han, Y. W.; Song, H. J.; Jeon, S. J.; Lee, H. S.; Ko, E. J.; Song, C. E.; Sung, T. H.; Moon, D. K. Excellent Carrier Transport Materials Produced by Controlled Molecular Stacking and Their Application in Flexible Organic Electronic Devices. *J. Mater. Chem. A* **2019**, *7*, 14790−14805.

(2) Han, Y. W.; Jung, C. H.; Lee, H. S.; Jeon, S. J.; Moon, D. K. High-Performance Nonfullerene Organic Photovoltaics Applicable for Both Outdoor and Indoor Environments through Directional Photon Energy Transfer. *ACS Appl. Mater. Interfaces* **2020**, *12*, 38470−38482.

(3) An, C.; Zheng, Z.; Hou, J. Recent Progress in Wide Bandgap Conjugated Polymer Donors for High-Performance Nonfullerene Organic Photovoltaics. *Chem. Commun.* **2020**, *56*, 4750−4760.

(4) Park, S.; Kim, T.; Yoon, S.; Koh, C. W.; Woo, H. Y.; Son, H. J. Progress in Materials, Solution Processes, and Long-Term Stability for Large-Area Organic Photovoltaics. *Adv. Mater.* **2020**, *32*, 1−29.

(5) Karki, A.; Gillett, A. J.; Friend, R. H.; Nguyen, T. Q. The Path to 20% Power Conversion Efficiencies in Nonfullerene Acceptor Organic Solar Cells. *Adv. Energy Mater.* **2021**, *11*, 1−30.

(6) Kini, G. P.; Jeon, S. J.; Moon, D. K. Design Principles and Synergistic Effects of Chlorination on a Conjugated Backbone for Efficient Organic Photovoltaics: A Critical Review. *Adv. Mater.* **2020**, *32*, 1−38.

(7) Jeon, S. J.; Han, Y. W.; Moon, D. K. 13.9%-Efficiency and Eco-Friendly Nonfullerene Polymer Solar Cells Obtained by Balancing Molecular Weight and Solubility in Chlorinated Thiophene-Based Polymer Backbones. *Small* **2019**, *15*, 1−11.

(8) Kini, G. P.; Jeon, S. J.; Moon, D. K. Latest Progress on Photoabsorbent Materials for Multifunctional Semitransparent Organic Solar Cells. *Adv. Funct. Mater.* **2021**, *31*, 1−32.

(9) Han, S.; Deng, Y.; Han, W.; Ren, G.; Song, Z.; Liu, C.; Guo, W. Recent Advances of Semitransparent Organic Solar Cells. *Sol. Energy* **2021**, *225*, 97−107.

(10) Chinese Journal of Chemistry - 2021 - Yang - Solution-Processed Silver Nanowire as Flexible Transparent Electrodes in.Pdf.

(11) Wang, H. C.; Cheng, P.; Tan, S.; Chen, C. H.; Chang, B.; Tsao, C. S.; Chen, L. Y.; Hsieh, C. A.; Lin, Y. C.; Cheng, H. W.; Yang, Y.; Wei, K. H. Sequential Deposition of Donor and Acceptor Provides High-Performance Semitransparent Organic Photovoltaics Having a Pseudo p−i−n Active Layer Structure. *Adv. Energy Mater.* **2021**, *11*, No. 2003576.

(12) Zhang, S.; Qin, Y.; Zhu, J.; Hou, J. Over 14% Efficiency in Polymer Solar Cells Enabled by a Chlorinated Polymer Donor. *Adv. Mater.* **2018**, *30*, 1−7.

(13) Yuan, J.; Zhang, Y.; Zhou, L.; Zhang, G.; Yip, H. L.; Lau, T. K.; Lu, X.; Zhu, C.; Peng, H.; Johnson, P. A.; Leclerc, M.; Cao, Y.; Ulanski, J.; Li, Y.; Zou, Y. Single-Junction Organic Solar Cell with over 15% Efficiency Using Fused-Ring Acceptor with Electron-Deficient Core. *Joule* **2019**, *3*, 1140−1151.

(14) Cheng, J.; Xie, F.; Liu, Y.; Sha, W. E. I.; Li, X.; Yang, Y.; Choy, W. C. H. Efficient Hole Transport Layers with Widely Tunable Work Function for Deep HOMO Level Organic Solar Cells. *J. Mater. Chem. A* **2015**, *3*, 23955−23963.

(15) Lee, E. J.; Heo, S. W.; Han, Y. W.; Moon, D. K. An Organic-Inorganic Hybrid Interlayer for Improved Electron Extraction in Inverted Polymer Solar Cells. *J. Mater. Chem. C* **2016**, *4*, 2463−2469.

(16) Han, Y. W.; Choi, J. Y.; Lee, Y. J.; Ko, E. J.; Choi, M. H.; Suh, I. S.; Moon, D. K. Vertical Phase Separation for Highly Efficient Organic Solar Cells Incorporating Conjugated-Polyelectrolytes. *Adv. Mater. Interfaces* **2019**, *6*, 1−15.

(17) Han, Y. W.; Lee, E. J.; Joo, J.; Park, J.; Sung, T. H.; Moon, D. K. Photon Energy Transfer by Quantum Dots in Organic-Inorganic Hybrid Solar Cells through FRET. *J. Mater. Chem. A* **2016**, *4*, 10444−10453.

(18) Chen, M. H.; Lin, Y. C.; She, N. Z.; Huang, Y. Y.; Lin, D. L.; Luo, C. W. Performance and Stability Improvement in Organic Photovoltaics Using Non-Toxic PEIE Interfacial Layers. *Org. Electron.* **2021**, *98*, No. 106303.

(19) Park, H. S.; Han, Y. W.; Lee, H. S.; Jeon, S. J.; Moon, D. K. 13.2% Efficiency of Organic Solar Cells by Controlling Interfacial Resistance Resulting from Well-Distributed Vertical Phase Separation. *ACS Appl. Energy Mater.* **2020**, *3*, 3745−3754.

(20) Xiong, S.; Hu, L.; Hu, L.; Sun, L.; Qin, F.; Liu, X.; Fahlman, M.; Zhou, Y. 12.5% Flexible Nonfullerene Solar Cells by Passivating the Chemical Interaction Between the Active Layer and Polymer Interfacial Layer. *Adv. Mater.* **2019**, *31*, 1−7.

(21) Bai, Y.; Zhao, C.; Shi, R.; Wang, J.; Wang, F.; Hayat, T.; Alsaedi, A.; Tan, Z. Novel Cathode Buffer Layer of $Al(Acac)_3$enables Efficient, Large Area and Stable Semi-Transparent Organic Solar Cells. *Mater. Chem. Front.* **2020**, *4*, 2072−2080.

(22) Su, M. S.; Kuo, C. Y.; Yuan, M. C.; Jeng, U. S.; Su, C. J.; Wei, K. H. Improving Device Efficiency of Polymer/Fullerene Bulk Heterojunction Solar Cells through Enhanced Crystallinity and Reduced Grain Boundaries Induced by Solvent Additives. *Adv. Mater.* **2011**, *23*, 3315−3319.

(23) Liu, C. M.; Su, Y. W.; Jiang, J. M.; Chen, H. C.; Lin, S. W.; Su, C. J.; Jeng, U. S.; Wei, K. H. Complementary Solvent Additives Tune the Orientation of Polymer Lamellae, Reduce the Sizes of Aggregated Fullerene Domains, and Enhance the Performance of Bulk Heterojunction Solar Cells. *J. Mater. Chem. A* **2014**, *2*, 20760−20769.

(24) Yuan, J.; Zou, Y. The History and Development of Y6. *Org. Electron.* **2022**, *102*, No. 106436.

(25) Advanced Energy Materials − 2022 - Perdig N-Toro - Understanding the Role of Order in Y-Series Non-Fullerene Solar Cells to. Pdf.

(26) Guo, B.; Yin, Q.; Zhou, J.; Li, W.; Zhang, K.; Li, Y. Semiconductive Polymer-Doped PEDOT with High Work Function, Conductivity, Reversible Dispersion, and Application in Organic Solar Cells. *ACS Sustainable Chem. Eng.* **2019**, *7*, 8206−8214.
(27) Tang, Y.; Sun, H.; Wu, Z.; Zhang, Y.; Zhang, G.; Su, M.; Zhou, X.; Wu, X.; Sun, W.; Zhang, X.; Liu, B.; Chen, W.; Liao, Q.; Woo, H. Y.; Guo, X. A New Wide Bandgap Donor Polymer for Efficient Nonfullerene Organic Solar Cells with a Large Open-Circuit Voltage. *Adv. Sci.* **2019**, *6*, 1−10.
(28) Guo, Q.; Li, F.; Li, J.; Xiao, Y.; Zuo, K.; Tang, A.; Zhang, B.; Zhou, E. Modulating the Middle and End-Capped Units of A2-A1-D-A1-A2 Type Non-Fullerene Acceptors for High VOC Organic Solar Cells. *Org. Electron.* **2021**, *95*, No. 106195.
(29) Maisch, P.; Eisenhofer, L. M.; Tam, K. C.; Distler, A.; Voigt, M. M.; Brabec, C. J.; Egelhaaf, H. J. A Generic Surfactant-Free Approach to Overcome Wetting Limitations and Its Application to Improve Inkjet-Printed P3HT:Non-Fullerene Acceptor PV. *J. Mater. Chem. A* **2019**, *7*, 13215−13224.
(30) Abdulrazzaq, O.; Bourdo, S. E.; Woo, M.; Saini, V.; Berry, B. C.; Ghosh, A.; Biris, A. S. Comparative Aging Study of Organic Solar Cells Utilizing Polyaniline and PEDOT:PSS as Hole Transport Layers. *ACS Appl. Mater. Interfaces* **2015**, *7*, 27667−27675.
(31) Li, Q.; Sun, Y.; Yang, C.; Liu, K.; Islam, M. R.; Li, L.; Wang, Z.; Qu, S. Optimizing the Component Ratio of PEDOT:PSS by Water Rinse for High Efficiency Organic Solar Cells over 16.7%. *Sci. Bull.* **2020**, *65*, 747−752.
(32) Yi, M.; Jang, W.; Wang, D. H. Controlled PH of PEDOT:PSS for Reproducible Efficiency in Inverted Perovskite Solar Cells: Independent of Active Area and Humidity. *ACS Sustainable Chem. Eng.* **2019**, *7*, 8245−8254.
(33) Meng, Y.; Hu, Z.; Ai, N.; Jiang, Z.; Wang, J.; Peng, J.; Cao, Y. Improving the Stability of Bulk Heterojunction Solar Cells by Incorporating PH-Neutral PEDOT:PSS as the Hole Transport Layer. *ACS Appl. Mater. Interfaces* **2014**, *6*, 5122−5129.
(34) Norrman, K.; Madsen, M. V.; Gevorgyan, S. A.; Krebs, F. C. Degradation Patterns in Water and Oxygen of an Inverted Polymer Solar Cell. *J. Am. Chem. Soc.* **2010**, *132*, 16883−16892.
(35) Han, Y. W.; Jeon, S. J.; Lee, H. S.; Park, H.; Kim, K. S.; Lee, H.-W.; Moon, D. K. Evaporation-Free Nonfullerene Flexible Organic Solar Cell Modules Manufactured by An All-Solution Process. *Adv. Energy Mater.* **2019**, *9*, No. 1902065.
(36) Zhao, Z.; Wu, Q.; Xia, F.; Chen, X.; Liu, Y.; Zhang, W.; Zhu, J.; Dai, S.; Yang, S. Improving the Conductivity of PEDOT:PSS Hole Transport Layer in Polymer Solar Cells via Copper(II) Bromide Salt Doping. *ACS Appl. Mater. Interfaces* **2015**, *7*, 1439−1448.
(37) Yang, K.; Chen, S.; Fu, J.; Jung, S.; Ye, J.; Kan, Z.; Hu, C.; Yang, C.; Xiao, Z.; Lu, S.; Sun, K. Molecular Lock Induced by Chloroplatinic Acid Doping of PEDOT:PSS for High-Performance Organic Photovoltaics. *ACS Appl. Mater. Interfaces* **2020**, *12*, 30954−30961.
(38) Zhang, L.; Yang, K.; Chen, R.; Zhou, Y.; Chen, S.; Zheng, Y.; Li, M.; Xu, C.; Tang, X.; Zang, Z.; Sun, K. The Role of Mineral Acid Doping of PEDOT:PSS and Its Application in Organic Photovoltaics. *Adv. Electron. Mater.* **2020**, *6*, 29−33.
(39) Wang, J.; Zheng, Z.; Zhang, D.; Zhang, J.; Zhou, J.; Liu, J.; Xie, S.; Zhao, Y.; Zhang, Y.; Wei, Z.; Hou, J.; Tang, Z.; Zhou, H. Regulating Bulk-Heterojunction Molecular Orientations through Surface Free Energy Control of Hole-Transporting Layers for High-Performance Organic Solar Cells. *Adv. Mater.* **2019**, *31*, 1−10.
(40) Solar RRL - 2021 - Kang - A PH-Neutral Polyelectrolyte Hole Transport Layer for Improved Energy Band Structure at the Anode.Pdf.
(41) Chiou, G. C.; Lin, M. W.; Lai, Y. L.; Chang, C. K.; Jiang, J. M.; Su, Y. W.; Wei, K. H.; Hsu, Y. J. Fluorene Conjugated Polymer/Nickel Oxide Nanocomposite Hole Transport Layer Enhances the Efficiency of Organic Photovoltaic Devices. *ACS Appl. Mater. Interfaces* **2017**, *9*, 2232−2239.
(42) Zheng, Z.; Hu, Q.; Zhang, S.; Zhang, D.; Wang, J.; Xie, S.; Wang, R.; Qin, Y.; Li, W.; Hong, L.; Liang, N.; Liu, F.; Zhang, Y.; Wei, Z.; Tang, Z.; Russell, T. P.; Hou, J.; Zhou, H. A Highly Efficient Non-Fullerene Organic Solar Cell with a Fill Factor over 0.80 Enabled by a Fine-Tuned Hole-Transporting Layer. *Adv. Mater.* **2018**, *30*, 1−9.
(43) Cheng, F.; Wu, Y.; Shen, Y.; Cai, X.; Li, L. Enhancing the Performance and Stability of Organic Solar Cells Using Solution Processed MoO3 as Hole Transport Layer. *RSC Adv.* **2017**, *7*, 37952−37958.
(44) Kang, Q.; Yang, B.; Xu, Y.; Xu, B.; Hou, J. Printable MoOx Anode Interlayers for Organic Solar Cells. *Adv. Mater.* **2018**, *30*, 1−7.
(45) Murase, S.; Yang, Y. Solution Processed MoO 3 Interfacial Layer for Organic Photovoltaics Prepared by a Facile Synthesis Method. *Adv. Mater.* **2012**, *24*, 2459−2462.
(46) Choy, W. C. H.; Zhang, D. Solution-Processed Metal Oxides as Efficient Carrier Transport Layers for Organic Photovoltaics. *Small* **2016**, *12*, 416−431.
(47) Han, Y. W.; Lee, H. S.; Moon, D. K. Printable and Semitransparent Nonfullerene Organic Solar Modules over 30 Cm2Introducing an Energy-Level Controllable Hole Transport Layer. *ACS Appl. Mater. Interfaces* **2021**, *13*, 19085−19098.
(48) Li, Y.; Wang, Y.; Zuo, Q.; Li, B.; Li, Y.; Cai, W.; Qing, J.; Li, Y.; Liu, X.; Shi, J.; Hou, L. Efficient Hole Transport Layer for Organic Solar Cell Based on Exfoliated-MoS $_2$ Doped PEDOT. *SSRN Electron. J.* **2022**, No. 3987633.
(49) Kim, J.; Ouyang, D.; Lu, H.; Ye, F.; Guo, Y.; Zhao, N.; Choy, W. C. H. High Performance Flexible Transparent Electrode via One-Step Multifunctional Treatment for Ag Nanonetwork Composites Semi-Embedded in Low-Temperature-Processed Substrate for Highly Performed Organic Photovoltaics. *Adv. Energy Mater.* **2020**, *10*, 1−12.
(50) Ali, A. M.; Said, D. A.; Khayyat, M.; Boustimi, M.; Seoudi, R. Improving the Efficiency of the Organic Solar Cell (CuPc/C60) via PEDOT: PSS as a Photoconductor Layer Doped by Silver Nanoparticles. *Results Phys.* , *2020* (), 102819, DOI: 10.1016/j.rinp.2019.102819.
(51) Jiang, X.; Sun, L.; Wang, W.; Qin, F.; Xie, C.; Hu, L.; Zhou, Y. 10 Cm2 Nonfullerene Solar Cells with Efficiency over 10% Using H: $XMoO_3$-Assisted Growth of Silver Electrodes with a Low Threshold Thickness of 4 Nm. *J. Mater. Chem. A* **2020**, *8*, 69−76.
(52) Yang, Y.; Kang, Q.; Liao, Q.; Zheng, Z.; He, C.; Xu, B.; Hou, J. Inorganic Molecular Clusters with Facile Preparation and Neutral PH for Efficient Hole Extraction in Organic Solar Cells. *ACS Appl. Mater. Interfaces* **2020**, *12*, 39462−39470.
(53) Dong, J.; Guo, J.; Wang, X.; Dong, P.; Wang, Z.; Zhou, Y.; Miao, Y.; Zhao, B.; Hao, Y.; Wang, H.; Xu, B.; Yin, S. A Low-Temperature Solution-Processed CuSCN/Polymer Hole Transporting Layer Enables High Efficiency for Organic Solar Cells. *ACS Appl. Mater. Interfaces* **2020**, *12*, 46373−46380.
(54) Han, Y. W.; Jeon, S. J.; Choi, J. Y.; Kim, J. H.; Moon, D. K. Highly Efficient Ternary Solar Cells of 10.2% with Core/Shell Quantum Dots via FRET Effect. *Sol. RRL* **2018**, *2*, 1−11.
(55) He, Z.; Zhong, C.; Huang, X.; Wong, W. Y.; Wu, H.; Chen, L.; Su, S.; Cao, Y. Simultaneous Enhancement of Open-Circuit Voltage, Short-Circuit Current Density, and Fill Factor in Polymer Solar Cells. *Adv. Mater.* **2011**, *23*, 4636−4643.
(56) Adv Funct Materials - 2020 - Yang - Boosting Performance of Non-Fullerene Organic Solar Cells by 2D G-C3N4 Doped PEDOT PSS.Pdf.
(57) Wang, J.; Wang, J.; Yu, H.; Yu, H.; Yu, H.; Hou, C.; Zhang, J. Solution-Processable PEDOT:PSS:α-In_2Se_3 with Enhanced Conductivity as a Hole Transport Layer for High-Performance Polymer Solar Cells. *ACS Appl. Mater. Interfaces* **2020**, *12*, 26543−26554.
(58) Choi, J. Y.; Han, Y. W.; Jeon, S. J.; Ko, E. J.; Moon, D. K. Introduction of Co-Additives to Form Well Dispersed Photoactive Layer to Improve Performance and Stability of Organic Solar Cells. *Sol. Energy* , *2019* (), 1−12, DOI: 10.1016/j.solener.2019.03.093.
(59) Thomas, J. P.; Shi, Q.; Abd-Ellah, M.; Zhang, L.; Heinig, N. F.; Leung, K. T. Charge Transfer in Nanowire-Embedded PEDOT:PSS and Planar Heterojunction Solar Cells. *ACS Appl. Mater. Interfaces* **2020**, *12*, 11459−11466.

https://doi.org/10.1021/acsaem.2c00960
ACS Appl. Energy Mater. XXXX, XXX, XXX−XXX

(60) Advanced Sustainable Systems - 2020 - Alharbi - A General Approach of Adjusting the Surface-Free Energy of the Interfacial.Pdf.
(61) Wang, Y.; Zhu, C.; Pfattner, R.; Yan, H.; Jin, L.; Chen, S.; Molina-Lopez, F.; Lissel, F.; Liu, J.; Rabiah, N. I.; Chen, Z.; Chung, J. W.; Linder, C.; Toney, M. F.; Murmann, B.; Bao, Z. A Highly Stretchable, Transparent, and Conductive Polymer. *Sci. Adv.* **2017**, *3*, 1−11.
(62) Solar RRL - 2020 - Mahmood - A Review of Grazing Incidence Small- and Wide-Angle X-Ray Scattering Techniques for Exploring.Pdf.
(63) Li, J.; Qin, J.; Liu, X.; Ren, M.; Tong, J.; Zheng, N.; Chen, W.; Xia, Y. Enhanced Organic Photovoltaic Performance through Promoting Crystallinity of Photoactive Layer and Conductivity of Hole-Transporting Layer by V_2O_5 Doped PEDOT:PSS Hole-Transporting Layers. *Sol. Energy* **2020**, *211*, 1102−1109.
(64) Chen, S.; Liu, Y.; Zhang, L.; Chow, P. C. Y.; Wang, Z.; Zhang, G.; Ma, W.; Yan, H. A Wide-Bandgap Donor Polymer for Highly Efficient Non-Fullerene Organic Solar Cells with a Small Voltage Loss. *J. Am. Chem. Soc.* **2017**, *139*, 6298−6301.

https://doi.org/10.1021/acsaem.2c00960
ACS Appl. Energy Mater. XXXX, XXX, XXX−XXX